Check for updates

Advanced Energy Materials

ADVANCED ENERGY MATERIALS
www.advenergymat.de

RESEARCH ARTICLE OPEN ACCESS

Atomic Scale Ordering of Liquid Water at a Dynamic Pt(111) Interface Under Electrochemical Conditions Imaged by Electron Holography

Jonas Lindner[1] | Ulrich Ross[1,2] | Tobias Meyer[1] | Sung Sakong[3] | Axel Gross[3,4] | Michael Seibt[2] | Christian Jooss[1,5]

[1]Institute of Materials Physics, University of Goettingen, Goettingen, Lower Saxony, Germany | [2]4th Institute of Physics – Solids and Nanostructures, University of Goettingen, Goettingen, Lower Saxony, Germany | [3]Institute of Theoretical Chemistry, University Ulm, Ulm, Germany | [4]Elementary Processes, Helmholtz Institute Ulm (HIU), Ulm, Germany | [5]International Center for Advanced Studies of Energy Conversion (ICASEC), University of Goettingen, Goettingen, Lower Saxony, Germany

Correspondence: Christian Jooss (cjooss@gwdg.de)

Received: 10 October 2025 | **Revised:** 11 December 2025 | **Accepted:** 8 January 2026

Keywords: ab-initio molecular dynamics | electric double layer | interfacial water-ordering | off-axis electron holography

ABSTRACT

Imaging atomic structure and electric fields of the electric double layer at electrode-water interfaces is essential for understanding electrochemical reactions. The wave properties of electrons in an environmental transmission electron microscope were used to reconstruct the atomic scale electric potentials of a platinum (111) interface in water by phase shifting electron holography. This progress allowed the observation of ordered water layers at the dynamic state of the platinum (111) surface and the water reorganization under applied electric potentials. The obtained projected electric potential of the Pt-water interface is quantitatively compared to ab-initio molecular dynamics simulations, revealing an extended ordered water region. We conclude that the potential drop at the Pt -H_2O interface is mainly carried by the polarization field of the ordered water structure. The impact of different surface Pt configurations and the presence of adsorbates on the ordered structure are discussed.

1 | Introduction

In 1879, Helmholtz [1] introduced the concept of the electrochemical double layer (EDL) that forms at the interface between an electrode and an electrolyte as a result of the chemical equilibrium of electrons and ions. His space charge region model has been later extended by Gouy and Chapman [2] as well as by Stern [3] by subdividing the electrolyte into the inner layer of adsorbed ions or molecules and the outer layer of solvated ions, which can merge into a diffuse layer. The EDL is of pre-eminent importance for all electrochemical processes at the solid-liquid interface since its dynamical structure determines the energy landscape along which electron transfer processes and reaction products proceed. At aqueous interfaces, water molecules have different properties than their bulk counterparts, due to the impact of the surface on the hydrogen bonding network [4]. In particular, the balance between hydrogen bonding parallel to the surface and water adsorption leads to orientation and ordering of the first layer [5, 6]. In the absence of ions, the electric field induced by surface charges predominantly needs to be balanced by the orientation of water dipoles. This induces an orientational order that persists over a certain depth into the bulk [7]. The detailed dependence on charge, surface structure, presence of ions or foreign adsorbates is far from being well understood, although the resulting change of the hydrogen bonding network and arrangement of water

Jonas Lindner and Ulrich Ross contributed equally to this work.

This is an open access article under the terms of the Creative Commons Attribution License, which permits use, distribution and reproduction in any medium, provided the original work is properly cited.

© 2026 The Author(s). *Advanced Energy Materials* published by Wiley-VCH GmbH

dipoles are expected to have a strong impact on electro-catalytic reactions [8].

One particular aspect is the possible impact of the dynamic state of electrode surfaces on ordering. Dynamical states electrode water interfaces have been observed previously for many systems and affect coordination chemistry of the active sites [9–15]. To gain insight into the water dipole network structure close to an electrified interface is thus of tremendous importance for the development of atomic scale EDL models and electron-driven reactions. However, after over 100 years, the development of a realistic atomistic description of the different parts of the EDL, beyond the simple mean field models, remains an unparalleled challenge [16]. This is even true when applying state-of-the-art ab-initio molecular dynamics calculations, which have seen significant progress [8, 17–20]. The difficulty arises from the inherently fluctuating nature of the open system and the complex, multi-scale interplay among the solid, liquid, ionic, and electronic components at the interface.

Recent progress has been made by experiments, such as scanning probes, which give some insights into the rich variety of structures that water can adopt on a surface. In studies of ice far below the melting temperature, in-plane ordering of water has been observed on various surfaces, including noble metals, by scanning tunneling microscopy [21] and atomic force microscopy [22]. Particularly, the progress in 3D atomic force microscopy (3D-AFM) led to atomic-level images of the liquid-solid interface. Although 3D-AFM offered insights into the ordering of water layers normal to the surface under ambient conditions [23], deriving an accurate relationship between the force and the solvent density remains a great challenge [24].

In this study, we establish access to the atomic scale electric potentials at a Pt-water interface and its change upon biasing with 1 Angstrom spatial resolution. The atomic scale potentials are highly relevant for interfacial electron transfer processes and thus for understanding electrochemical reactions. We use phase-shifting electron holography (PS-EH) [25] to measure the phase shift of the electron wave due to the atomic electric potentials. This phase shift is reconstructed in an aberration-corrected environmental transmission electron microscope (ETEM) to observe the water-Pt(111) interface. Since the phase shift of the electron wave is proportional to the electric potential across the surface, it provides a direct measure of the potential oscillations at the atomic scale, which are mediated by the water structure, in contrast to density variations as revealed by 3D-AFM. The model electrochemical cell in the ETEM is a water film on the noble metal surface immersed in low-pressure water vapor, which can be biased in a two electrode setup. We selected the Pt(111) surface due to its fundamental relevance for catalysis. In this pressure range, a condensed water film forms on the Pt surface due to the effect of surface adsorption. Due to the absence of a bulk aqueous electrolyte, the ion concentration is low [26] and thus a change of surface charge is predominantly shielded by reorientation of water dipole layers, which are formed by the balance of surface absorption and hydrogen bonding. The main findings of our experiments are the presence of ordered water layers on a dynamic Pt (111) surface that extends over a range up to 7 Å from the surface. This range is larger than previously expected for flat noble metal surfaces based on ab-initio molecular dynamics (AIMD) [8, 17]. We directly image the change of the projected potential under application of an external bias, which is attributed to the reorientation of water molecules. This suggests that the major potential drop across the EDL is mediated by the oscillating dielectric polarization of the water dipoles. Furthermore, we combine AIMD and simulations of the phase shifts of the electron wave to compare the experimental data to ensemble-averaged theoretical structure predictions of the water network. Finally, the impact of surface adsorbates and impurities on the atomic scale electric potential is discussed.

2 | Results and Discussion

2.1 | Imaging the Pt(111)-Water Interface by Phase-Shifting Electron Holography

The as-prepared polycrystalline platinum flake is first characterized under high-vacuum conditions. The sample orientation is chosen such that the projected zone axis is Pt [110]. The front edge of the flake is faceted along Pt(111) planes. Following the high-vacuum characterization, the sample surface is treated in 1 mbar of oxygen under electron beam illumination and subsequently exposed to water vapor (see Figure S4). This results in a reconstructed surface for the investigation of water layers on Pt(111). Above an ambient pressure of $1 \cdot 10^{-7}$ mbar, a thin film of liquid water is formed due to the high absorption energy of water on metal surfaces. This film does not vary strongly in thickness with the chosen pressure over a wide range [27]. The pressure of 50 µbar of water vapor proved sufficient to form a liquid water layer, while conserving the electron coherence for PS-EH. More details can be found in the Experimental section. We first show the formation of an ordered liquid water layer on Pt(111) surface. In the as-prepared state in high vacuum, samples reveal some structural disorder most easily detectable in the two uppermost surface layers (Figure 1A,B) due to the typical damage resulting from ion-milling techniques for TEM sample preparation. After in situ oxygen treatment (see Note S1), highly ordered extended Pt(111) terraces were formed in the water environment as perfect objects for cross-sectional imaging. The interface between these facets and the liquid adsorbate layer possesses very little contrast in conventional high-resolution imaging of the modulus of the image wave (see Figure 1D). The phase of the complex object wave reconstructed by phase-shifting holography, however, provides clear signal with angstrom resolution as shown in Figure 1E. For thin samples, the phase of the wave is proportional to the scattering potential of the object projected along the electron beam [28, 29], i.e. spatial variations of the phase map reflect the spatial distribution of atoms. More precisely, for the adsorbate layer, we need to consider the high mobility of its constituents, implying that we measure its temporal average for typical recording times of 60–90 s required for a PS-EH series. In order to improve the signal-to-noise ratio, phase profiles perpendicular to Pt(111) facets can be obtained by averaging along the (111) planes as indicated by rectangles in Figure 1B,E. The resulting line profiles for (111) facets in vacuum and 50 µbar water vapor are shown in Figure 1C,F, respectively.

The reconstructed phase signals exhibit a pronounced qualitative difference between vacuum and water ambient, as indicated by

16146840, 0, Downloaded from https://advanced.onlinelibrary.wiley.com/doi/10.1002/aenm.202505756 by KIZ der Universitat Ulm, Wiley Online Library on [21/01/2026]. See the Terms and Conditions (https://onlinelibrary.wiley.com/terms-and-conditions) on Wiley Online Library for rules of use; OA articles are governed by the applicable Creative Commons License

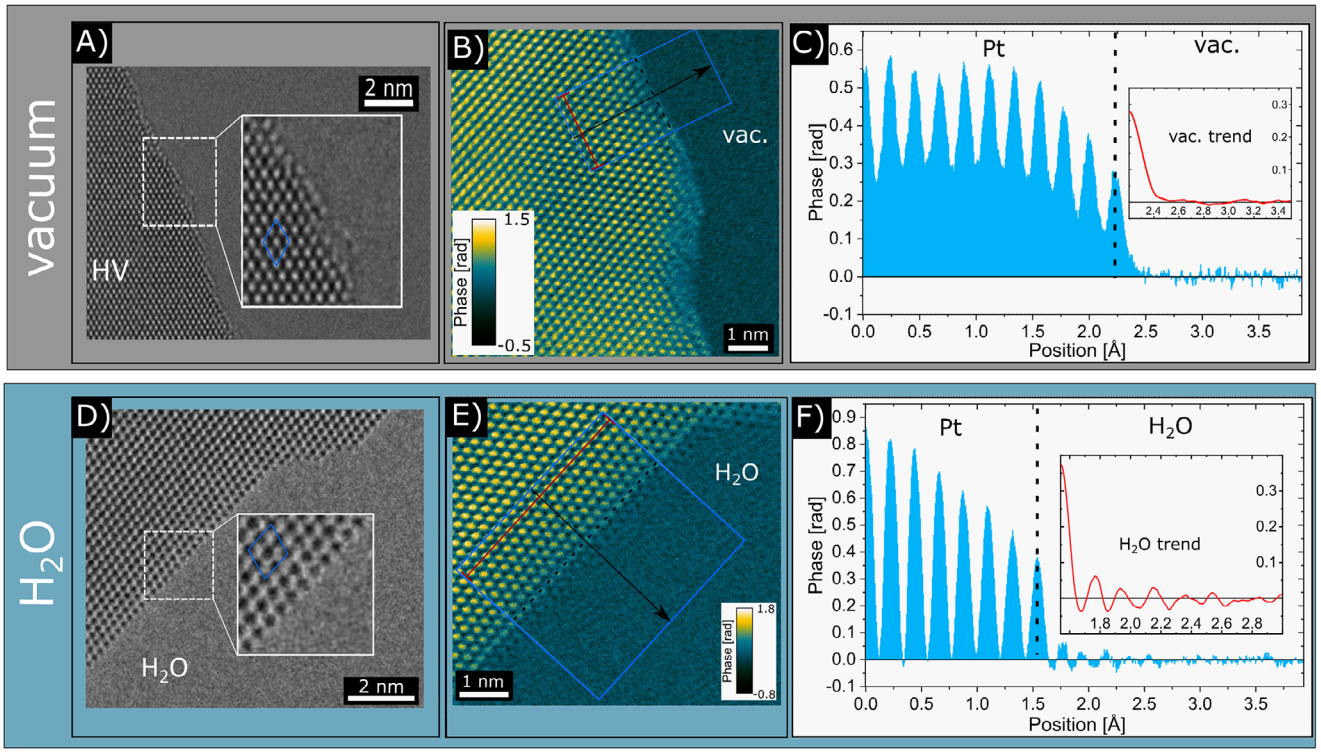

FIGURE 1 | Comparison of surface morphology and electron phase reconstructions of the Pt flake in vacuum and water at room temperature. (A) Pristine Pt surface after ion polishing, at 0 V external voltage in 10^{-7} mbar background pressure. The HR-TEM intensity image shows bright atom contrast for the Pt columns. Preparation-induced disorder at the surface up to the third plane is observed. (B) Reconstructed phase image by phase-shifting electron holography. First order aberrations were numerically corrected. (C) Vacuum phase profile perpendicular to the (111) planes, periodically averaged over 2.0 nm as indicated by the red bar in (B). The signal beyond the Pt edge (dashed line) shows a smooth transition into the vacuum background. The non-zero phase signal between the planes is attributed to the contribution from the amorphous regions. (D) Ordered Pt surface in 50 μbar water vapor. The high resolution-TEM intensity image was recorded under dark atom contrast conditions. A crystalline surface was formed in water after oxygen exposure, which shows faceted (111) planes. (E) Reconstructed phase image in water. (F) Phase profile perpendicular to the (111) planes as in C), with an averaging width of 4.2 nm. Oscillations of the phase signal are visible in the first 7 Å of the water region, suggesting the presence of ordered water layers along the surface normal direction. The Insets in (C) and (F) show a magnified view of the signal at the surface, smoothed by an SG-filter.

the insets in Figure 1C,F. For Pt(111) facets in vacuum, the phase signal smoothly decays from the top Pt layer into the background phase noise (σ_{vac} = 13 mrad) within about 3 Å. In the presence of water vapor, the phase spatially oscillates above the platinum surface. We take these phase oscillations as strong experimental evidence for the presence of ordered water layers since they are absent in high-vacuum. The outer extent of the water film is not visible due to its diffuse transition into the water vapor. In this case, again by comparing the signal to the noise level measured far away from the Pt(111) surface (σ_{H2O} = 11 mrad), the thickness of the ordered adsorbate layer is estimated as 7 Å.

2.2 | Pt Ad-Atom Surface Dynamics in Water

In order to gain further insight into the surface structure and dynamics, a more quantitative analysis is needed. Considering the low activation energy of Pt surface ad-atom diffusion on Pt(111) in the range of 0.13 to 0.25 eV [30], Pt ad-atoms are expected to show very fast thermally activated surface hopping, with hopping rates of nanoseconds, which are not accessible by our setup. Surprisingly, time-resolved high-resolution TEM imaging with 2.5 frames per second indicated a dynamic state of the Pt(111) surface in water.

Figure 2A shows the time-averaged series with Pt(111) layers labeled L_0 – L_4. It turns out that for layers L1 – L4, the effect of time averaging is, as expected, the reduction of noise. In contrast, layer L_0 exhibits lateral blurring of the image intensity, which provides evidence for the underlying atomic structure to be dynamic on the time scale of the recorded image series, see also [31]. This statement is also supported by the comparison of the image intensity in L_0 on shorter time averages of 14 frames (5.6 s). Figure 2C shows the surface at two selected times. The columns with the highest intensity are marked in both images. For different times, different columns show the highest intensity, i.e., a change of the number of platinum atoms in the specific column over time (see Note S2 for more details).

Similarly, the measured phase of the complex object wave represents a time average since typically 60–90 s is required to record the PS-EH series used for phase reconstruction. Hence, as a second step, a spatially averaged phase is shown in Figure 2B, again exhibiting a blurred signal in layer L_0 and noise reduction in the remaining layers. As a final important observation, we note that despite the blurring of the maxima at the positions of the surface atoms, their positions can still be extrapolated from the fcc symmetry of the bulk lattice in Figure 2A,B. This is evidenced by comparing the unit cells in the bulk region and

16146840, 0, Downloaded from https://advanced.onlinelibrary.wiley.com/doi/10.1002/aenm.202505756 by KIZ der Universitat Ulm, Wiley Online Library on [21/01/2026]. See the Terms and Conditions (https://onlinelibrary.wiley.com/terms-and-conditions) on Wiley Online Library for rules of use; OA articles are governed by the applicable Creative Commons License

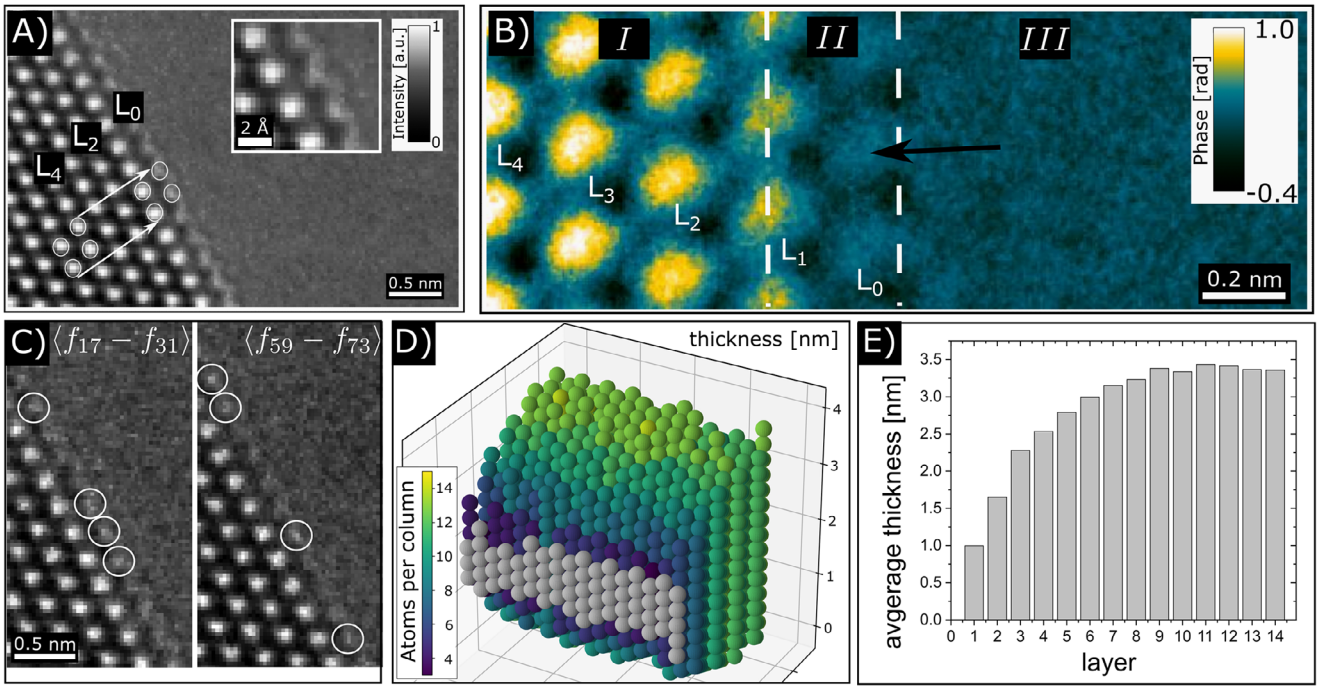

FIGURE 2 | Analysis of surface dynamics and specimen thickness. (A) Time average of in situ HR-TEM series from the Pt (111) surface in H_2O. Dynamic surface regions L_0 show a blurred contrast. (B) Averaged reconstructed phase signal. The image in (B) is color-coded to represent the platinum columns in yellow. For this lateral averaging the super cell was defined as an area of 2 nm × 0.7 nm, which contains periodically repeated information of seven super cells. Region I shows the atomic columns of bulk platinum. The thickness decreases toward the surface, layers are counted from the surface. The phase signal at L_0 corresponds to the dynamic layer in (A), showing a higher signal at FCC positions as highlighted by the circles in (A) and the black arrow. (C) Subset time average of 14 frames (5.6 s) of the in situ movie at different initial times (frame sets). The most intense columns in the dynamic surface layer L_0 are marked to guide the eye. The position-change of these signals indicates mobile platinum ad-atoms. (D) The number of atoms in a specific column is determined by averaging the phase signal in a unit cell around the column and compared to simulations, resulting in the surface model. Surface atoms in L_1 are marked in gray color. (E) The average layer thickness profile starting from L_1.

the surface. More quantitatively, distances and angles of these preferentially occupied surface sites of the (111) facets agree with the bulk fcc values within statistical error (see Note S3). Hence, as an intermediate result, we conclude that a dynamic layer (L_0) of Pt atoms forms on the (static) Pt(111) surface. This view is corroborated by excluding other adsorbates from the water environment as e.g. oxygen or Pt-O clusters. Previous work on Pt-O has shown that oxygen coverages exceeding 0.2 monolayers lead to displacement of the Pt surface atoms [32, 33]. This does not match the symmetry and positions of the phase maxima observed for L_0. Finally, calculating the phase-shift for a fully-filled oxygen column yields a signal far below the measured phase, yielding the most robust argument against the oxygen hypothesis and in favor of platinum.

For a quantitative analysis, we exploit the extraordinary phase sensitivity of our drift corrected phase shifting holography of $2\pi/452$ [25]. Combined with quantitative simulations of image waves, the projected potential can be extracted, or in other words, the number of atoms along an atomic column can be counted if the chemical species are known. For this purpose, we use the multislice method as implemented in ref. [34] which calculates the propagation of an incident electron plane-wave through a strong scattering object, taking into account diffuse scattering by lattice vibrations, and image aberrations. The number of atoms within each column of the experimental image is then determined from the comparison with the simulated phase. This is done by averaging the phase within a unit area in order to reduce noise, and correlating this with the simulated signals for a model surface with various thicknesses along the beam (see Experimental Section). The best-matching local structure of the platinum edge, and the average column thickness of each layer, are depicted in Figure 2D,E, respectively. The topmost static platinum layer L_1 is shaded in (D) for clarity. It consists of 3–5 atoms in each column, corresponding to an average thickness of 1 nm. This somewhat preliminary procedure of quantitatively determining the local specimen thickness of the static part of the Pt(111) facet is easily extended to the dynamic layer (L0) and yields a phase signal of 65 mrad, which is below the calculated contribution of a single static platinum atom of 135 mrad. In conjunction with the positions of the surface sites, this is thus consistent with an average occupation of 0.5 Pt per column of 1 nm thickness, equivalent to an average coverage of 1/8. Hence, we attribute the dynamic surface layer to mobile Pt ad-atoms based on the identified fcc-sites and phase signal height (see Note S4). We interpret the visible Pt surface fluctuations in water on a millisecond time scale and their absence in high vacuum as a slow-down of the surface dynamics of Pt ad-atoms [35]. We attribute this to interactions with water adsorbates that reduce the mobility of the ad-atoms (see Section 2.6).

16146840, 0, Downloaded from https://advanced.onlinelibrary.wiley.com/doi/10.1002/aenm.202505756 by KIZ der Universitat Ulm, Wiley Online Library on [21/01/2026]. See the Terms and Conditions (https://onlinelibrary.wiley.com/terms-and-conditions) on Wiley Online Library for rules of use; OA articles are governed by the applicable Creative Commons License

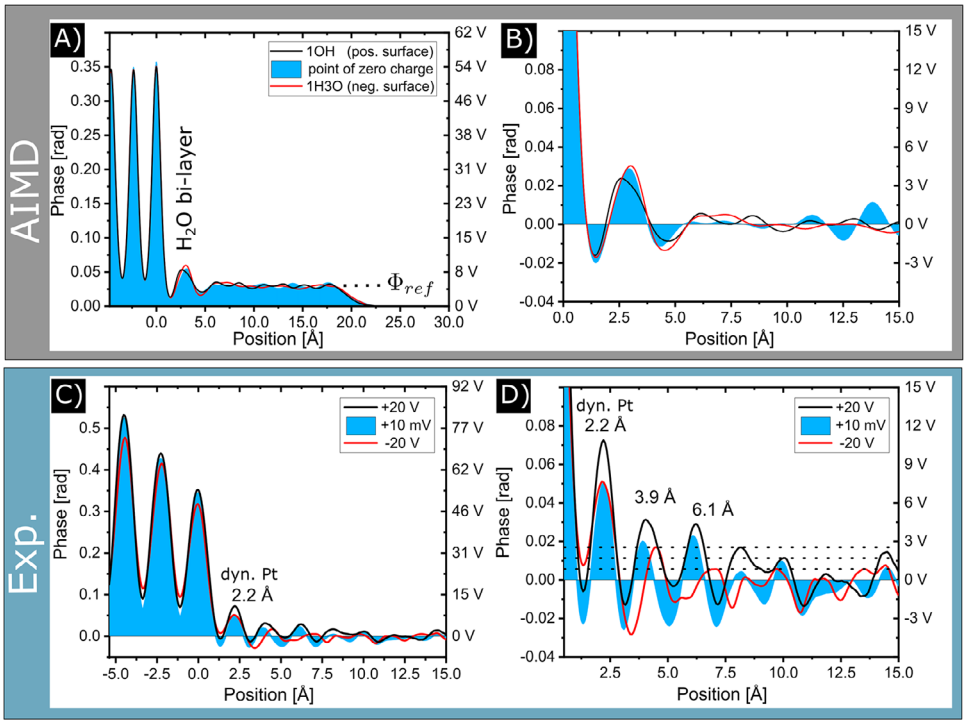

FIGURE 3 | Comparison of the phase signal predicted by AIMD-simulations of liquid water above a filled Pt surface, and water phase retrieved from the experiment. (A) Phase profile derived from AIMD data by multislice simulation. The surface charge was modified by adding OH^- or H_3O^+ ions to H_2O. (B) Inset of (A) to visualize the expected changes of the phase peak produced by the water bi-layer. Different states of surface charging are correlated to changes in the average orientation within the individual water dipole layers visible in the shifts of the peak position and height. The zero phase level in the inset was set to the mean projected potential of the 1 nm thick water film Φ_{ref}. (C) Changes of the phase distribution by variation of the external voltage [+20 V, +10 mV, −20 V] in the two-electrode experiment after signal filtering. [39] (D) Inset of (C) corresponding to the spatial scale of (B). The standard deviation of the filtered phase in the bulk water is indicated at 1, 2, and $3\sigma_{H2O}$ by dashed lines.

2.3 | Analysis of Ordered Water on the Dynamic Pt(111) Surface

The quantitative reconstruction of projected potentials allows us to measure the thickness of the platinum surface (Region I) and the average occupation of the dynamic surface layer by Pt ad-atoms (Region II), both shown in Figure 2. This is concluded exclusively from PS-EH experiments and the quantitative comparison to wavefunction- and image simulations. Based on the achieved high phase sensitivity in the holography reconstruction, we now analyze the phase oscillations visible in profiles across the surface. These peak features arise from the ordered structure of the water (Region III). The analysis is carried out by quantitative comparison of measured phase shifts to calculated phase shifts of ensemble-averaged water structures obtained by ab-initio molecular dynamic (AIMD) simulations (see Experimental Methods), as shown in Figure 3.

Compared to the Pt and Pt ad-atom signal, the magnitude of the oscillating phase signal is much lower. Disordered water molecules in the liquid or vapor do not generate any spatial phase contrast. In such regions the magnitude of the reconstructed phase is proportional to the difference in water density relative to a reference region and not to the absolute value of the mean inner potential of water. Since the water molecules in the liquid phase are highly dynamic and the diffusion and rotation of water occur in the order of pico-second time scale, the phase signal is the time average of the molecular positions. We consider the oscillations in Region III as experimental evidence of the ordering of water molecules above the mobile Pt ad-atom surface. Such formation of ordered water layers is well established by theoretical models such as [36–38]. Other candidates, such as ordered arrangements of impurities can, to a large extent, be ruled out, since they should also be visible in ambient other than H_2O, and can hardly stabilize in the presence of water vapor.

In a first step, the existing AIMD data of the Pt(111) surface from [36] is used to model an ordered liquid water layer above a solid slab, as well as the influence of the change in electrode potential on said ordering. Second, we then consider the influence of the experimentally observed additional partially-occupied layer of Pt ad-atoms on the expected signal in the ordered water layers and the corresponding reaction of the water network. The interface is modeled by 144 water molecules in contact with the (6×6) Pt(111) slab (see Experimental Section). In the simulation, the electrode potential is modified by varying the number of hydrogen atoms in the water film. Adding or removing a hydrogen atom leads to proton and hydroxide ion formation in the water film related to the transfer of one electron to (or from) the electrode and the electrode potential changes by ± 0.1 V.

A subset of the time-dependent AIMD configurations is used as *frozen-lattice* configurations for the transmission electron microscopy (TEM) exit-wave simulation [34] (see Note S5). This coupling of a dynamic model with multi-slice calculations offers two significant advantages over the typical Debye-Waller

16146840, 0, Downloaded from https://advanced.onlinelibrary.wiley.com/doi/10.1002/aenm.202505756 by KIZ der Universitat Ulm, Wiley Online Library on [21/01/2026]. See the Terms and Conditions (https://onlinelibrary.wiley.com/terms-and-conditions) on Wiley Online Library for rules of use; OA articles are governed by the applicable Creative Commons License

approach to the atomic displacements in frozen-lattice simulations. First, by using the time-dependent atomic positions from ab-initio calculations, the dynamic nature of the EDL is encoded in the result. The second advantage is that these simulations take the image formation mechanism in the microscope into account. It is thus possible to compare experiment and the simulated exit waves quantitatively.

The thickness of the simulated slab is adapted to the experimental surface-layer average of 1 nm as analyzed in Figure 2E. Since the effect of thermal motions and microscope aberrations on the image contrast are taken into account, this method allows us to quantitatively compare ensemble averages of simulated AIMD configurations to the reconstructed experimental phase in Figure 3. The potential profiles from simulations of the AIMD trajectories are shown in Figure 3A,B, while the experimental phase profiles are shown in Figure 3C,D. Each profile is extracted along the surface normal, and laterally averaged over the Pt(111) plane Figure 2D. The experimental profiles are smoothed by a peak conserving noise filter [39].

The water distribution from AIMD simulations shows a compact water layer formation at the extended interface. Despite the thermally induced orientational and positional fluctuations, the ensemble average over 40 ps reveals the presence of a water bi-layer with two distinct preferential 3D-orientations [36]. Close to the electrode, the O-H bonds point away from the surface, while they point toward the surface in the outer layer. A change in electrode potential by ±100 mV influences the likelihood of preferential orientations in this bi-layer, as shown in [40]. This results in small positional shifts of the ensemble average of the projected potential dominated by the oxygen density.

Due to the resolution limit of the microscope, these individual components of the bi-layer cannot be resolved. The simulated phase oscillations using AIMD trajectories thus exhibit an oscillation with the maximum peak height of 30 mrad at 3.0 Å in the profile, owing predominantly due to the projected atomic potential of the oxygen in the bi-layer.

2.4 | Change of Water Order Under Biasing

In order to change the electrode potential in the experiment, we apply external biases of +20 V, -20 V and 10 mV over an electrode gap of 4 µm. The magnitude of the biasing was at the upper limit of the instrumentation, in order to ensure positive, negative, and neutral surface polarization. The line profiles of the reconstructed experimental phase of the Pt water interface for different electrode biasing are shown in Figure 3C,D. The standard deviation in this region after noise filtering is σ_{H2O} = 6 mrad and includes the water vapor fluctuations, residual reconstruction artifacts (Fresnel modulations), shot noise, and the detector quantum efficiency of the CCD. The filtering hardly affects the dynamic platinum signal at 2.2 Å. The peak is exceeding $6 \cdot \sigma_{H2O}$. A comparison to the raw data is given in Note S6. In the region between 0 – 7 Å, up to two additional distinct peaks can be observed for all three external voltages. The peaks have a signal-to-noise ratio of $3–4 \cdot \sigma_{H2O}$. The position of the first peak varies from 3.9 Å to 4.4 Å depending on the applied external voltage. The position of the second peak shifts from 6.1 Å to 6.2 Å and vanishes for −20 V external potential. In contrast, the peak positions of both the Pt lattice and the dynamic layer remain constant. Fluctuations beyond 7 Å from the surface are largely uncorrelated and are below the confidence band of 3σ. The magnitude of the simulated phase peak for an ordered water bi-layer is in good agreement with the height of the measured peaks at 3.9 Å and 6.1 Å, above the mobile ad-atom layer. This suggests that the composition of these peaks is predominantly the result of ordered water molecules. The comparison between projected potentials derived from phase shifting holography and from ensemble-averaged AIMD structures agrees well in amplitude and degree of ordering, while the number of ordered peaks and their distances differ. A summary of the influence of the bias on peak positions and heights is shown in Table S2.

2.5 | The Influence of Surface Adsorbates

In order to answer whether the presence of the mobile ad-atom layer can explain these differences, we perform further AIMD simulations that include the influence of particles on the surface as shown in Figure 4. The models chosen are idealized configurations in order to investigate the general influence of decorating surface atoms. Four different surface configurations are considered: a clean flat surface, a hydrogen-saturated surface, and two surfaces with Pt ad-atoms at fcc sites at the coverage of 1/9.

These ad-atoms are either arranged to form tetramer islands or are maximally dispersed across the surface. An ad-atom coverage filling 1/9th of each surface site was chosen since building a model requires translational 6 × 6 symmetry in the supercell. This is close to the experimentally observed Pt surface coverage of 1/8. Transforming the rhombohedral AIMD supercell to the [110] zone axis and orthogonalizing for the multislice simulation includes adjusting the total thickness to the experimentally measured 1 nm. Since this adjustment includes partially cropping the repeated rhombohedral cell, it results in an ad-atom coverage of 1/6th of the fcc surface sites. Note that, on the order of the time-scale of the simulations, surface ad-atoms do not move between neighboring fcc surface sites.

The results of the phase simulation are shown in Figure 4E. Clearly, the presence and arrangement of ad-atoms have a strong influence on the distance and detailed structure of the first ordered water bi-layer. However, the simulations do not reproduce the experimentally found second water peak. The obtained position of the preferentially oriented water bi-layer depends on the configuration of the Pt ad-atoms. For the simulated flat Pt(111) surface, the position of the first water peak is at 2.7 Å, which is around 1 Å smaller than the experimental distance to the L_1 layer of the Pt(111) surface. The H-termination of the surface leads to a shift of first water peak position by around 1 Å to 3.7 Å compared to the pure Pt termination. In the case of 1/6 Pt surface coverage, the experimental position of the Pt ad-atom peak at 2.2 Å is well reproduced by the simulation. Consequently, the simulated water structure for the different Pt ad-atom configurations and surface terminations show that both have a strong influence on the structure of the ordered water.

16146840, 0, Downloaded from https://advanced.onlinelibrary.wiley.com/doi/10.1002/aenm.202505756 by KIZ der Universitat Ulm, Wiley Online Library on [21/01/2026]. See the Terms and Conditions (https://onlinelibrary.wiley.com/terms-and-conditions) on Wiley Online Library for rules of use; OA articles are governed by the applicable Creative Commons License

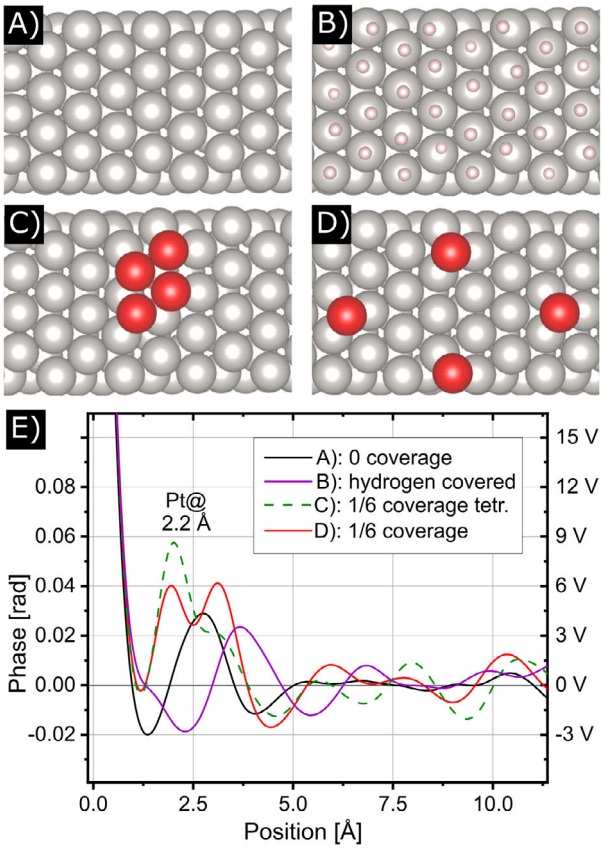

FIGURE 4 | Influence of hydrogen and Pt ad-atom coverage on the water structure as derived by AIMD simulations in comparison to the experiment. The position labels refer to positive peaks in the experimental signal. (A) No ad-atoms. (B) Hydrogen-covered surface. (C) Platinum tetramer at fcc positions formed by four platinum ad-atoms at 1/6 coverage. (D) Maximum spacing configuration of Pt ad-atoms on fcc sites at 1/6 coverage. (E) Simulated phase profiles for the four surface configurations in water in comparison to the experimental result at 10 mV.

2.6 | Discussion

While the amplitudes of the measured and the simulated phase oscillations of the ordered water layers match very well, there are differences between their positions which cannot be resolved by the presented surface configurations: The position of the first water ordering peak at 3.9 Å differs from that of the two simulated Pt ad-atom configurations, where the first water-related peaks are at 2.7 Å. Furthermore, the order-related phase oscillations in the experiment in Figure 3D extend up to 7 Å from the Pt L_1 surface layer and involve two phase oscillations of similar magnitude well above the $3 \cdot \sigma$ limit.

This is in contrast to the simulated phase oscillations based on AIMD structures, where only one significant oscillation evolves, which corresponds to one ordered bi-layer that extends up to 5 Å. Based on the AIMD simulations, we propose that the phase peaks in the experiment should result from a double bi-layer structure. Bilayers represent a more stable low-energy configuration compared to single layers due to the Hydrogen bond network [41]. However, the full width at half maximum of the first two phase oscillations of the experimental peaks is with 1.2 Å slightly narrower than the model prediction of 1.5 Å. An ordering of single water layers is, however, in contradiction to the distance of 2.2 Å between positive peaks that disagrees with the ordering of individual water layers at 3 and 6 Å [8].

The projected potential of the water is dominated by the oxygen atoms. Consequently, the phase oscillations in the ordered water region reflect the oxygen position in the ordered structure. Differences between measured and simulated distances of the phase peaks can have different origins: First, the experiment measures over long time scales, and includes many more Pt ad-atom configurations than considered by the simulation, due to the time scales Furthermore, our simulations show that the presence of adsorbed surface species, e.g. hydrogen or other possible contaminants can shift the first ordering peak compared to a clean surface. The experimentally observed larger extent of the ordered water layers may also hint at a stronger influence of long-range interactions on the water network than is currently considered by the simulation. Nevertheless, the magnitude of the electron phase shift due to the ordered projected potentials of water agrees very well with the prediction.

It is well-known that the electron beam impact of 300 keV electrons can induce artifacts in in situ TEM experiments. For example, inelastic collisions can drive surface atom kinetics as well as induce surface charging due to secondary electron emission [42, 43]. At the chosen beam current of 3000 $eÅ^{-2}$ s^{-1}, the measurement of beam-induced potential at Pt lamellas by using a piezo-controlled nanotip revealed a charging of about 10 mV, which we consider as irrelevant. The inelastic energy transfer to surface ad-atoms usually enhances the mobility of surface and ad-atoms both in vacuum and water. We observe HRTEM contrast changes on the millisecond time-scale in water, while the processes on the vacuum surface seem to be too fast to be recorded. This suggests that the water-induced change of the hopping barrier dominates over the electron beam impact on hopping rate. The AIMD simulations suggest that stabilizing interactions of ad-atoms or small clusters with the water layer slows down their mobility, similar to previous reports for step edges [44–46].

3 | Conclusions

By combining experimental electron phase reconstruction in two-electrode in situ ETEM holography with quantitative AIMD simulations, we derive the Pt(111)—H_2O interface structure, as summarized in Figure 5. This atomistic model establishes a dynamic nature of the electric double layer, where the degree of ordering of the water dipole network on a spatial extent of 7 Å is more long-range than previously expected. Based on the AIMD simulations, we suggest that the phase peaks in the experiment result from a double bi-layer structure, since the resulting hydrogen bonding network represents a minimum free energy configuration, and the amplitude as well as the width of the phase peaks are in reasonably good agreement with such a structure. There is a pronounced hopping of Pt ad-atom that is presumably slower in water than in high vacuum, since the ad-atoms are stabilized by the water ordering.

The strong change of the phase oscillations upon biasing indicates that the ordering of the orientational and spatial structure of the

16146840, 0, Downloaded from https://advanced.onlinelibrary.wiley.com/doi/10.1002/aenm.202505756 by KIZ der Universitat Ulm, Wiley Online Library on [21/01/2026]. See the Terms and Conditions (https://onlinelibrary.wiley.com/terms-and-conditions) on Wiley Online Library for rules of use; OA articles are governed by the applicable Creative Commons License

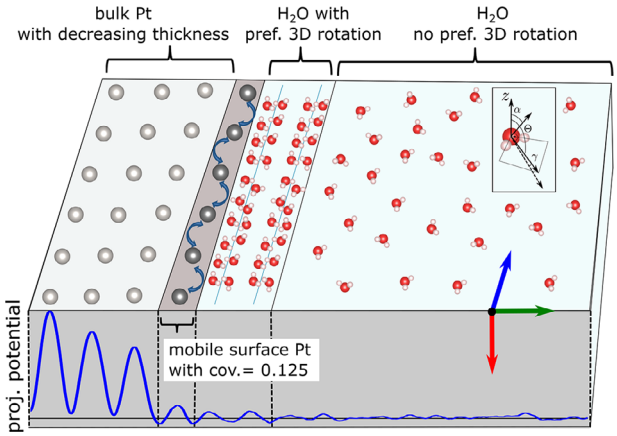

FIGURE 5 | Atomic scale model of the platinum-water interface derived by combined in situ ETEM experiments and AIMD simulations at zero voltage conditions. The bulk platinum shows a thickness gradient toward the specimen edge. On top of the (111)-surface, a dynamic platinum layer is found with a coverage of 1/8. The mobile platinum occupies the fcc lattice sites. From qualitative agreement of the phase oscillations with AIMD-analysis two bi-layers (≈7 Å) of preferential 3D-oriented water molecules are expected. The number of ordered layers and the specific orientations of the molecules are expected to differ from the result of [36] as discussed in the text. The bulk water shows no indications of preferential water orientation.

water network undergoes dramatic changes. Indeed, the potential drop at the Pt / H_2O interface is mainly carried by the dielectric polarization field of the water dipoles in the ordered region. That the potential drop and thus the local electric field is highest in the ordered water regions was already predicted by continuum models [47, 48]. In continuum models, it is the result of a strong field dependence of the dielectric constant due to reorientation of ordered water molecules. This leads to a strong localization of the potential drop at the ordered regions of the EDL close to the interface [49] underpinning the relevance of our in situ ETEM experiments for the understanding of the bias-dependent EDL, even in the absence of a diffuse layer of solvated ions. Furthermore, the atomic scale mapping of the electric potential at the interface reveals that the dielectric polarization field in the ordered water region possesses an oscillatory structure.

Our biasing-dependent experiments suggest that the reorganization of the water ordering will not only change the atomic scale potential drop but also how proton transfer is mediated to active sites. Indeed, the dynamically ordered structure of the hydrogen bonding network, in particular the hydrogen bonding density in the ordered layers has a huge impact on the proton mobility [50]. Since this influences the balance between proton supply and reaction demand, the biasing-induced restructuring of the network can not only affect the activity of a proton-coupled electron transfer reaction but also its selectivity as discussed in [51].

As shown by the AIMD simulations, the detailed structure of the atomic scale electric potential at the interface is influenced by surface termination, dynamic Pt ad-atoms, as well as possible impurities. Taking multiple possible initial surface configurations into account yields insights into the effect of Pt-ad-atoms on this ordering of water dipoles. In addition, the simulation of a hydrogen terminated surface shows that different chemical adsorbates can have a pronounced effect on the expected position and width of the phase signal resulting from a water bi-layer. The experimentally observed extent of the ordered water network, which is larger than initially suggested by AIMD simulations, is attributed to the pico-second time regime accessible by ab-initio methods and possible uncertainties in the treatment of long-range interactions. Furthermore, the chemical coverage of the surface (e.g., H-termination or possible other airborne species) can strongly influence the ordering.

4 | Experimental Section

4.1 | Experimental Setup and Specimen Preparation

The specimen was prepared by cold-rolling a high-purity polycrystalline platinum foil to ≈ 50 µm. A disc has been stamped out, which was further milled with low-energy argon ions (down to 300 V) in a Gatan precision ion polisher (PIPS). This led to the lowest edge thicknesses of a few nanometers. A four-contact electrical contacting MEMS chip (DENS Solutions Lightning) has then been prepared in the focused ion beam (Thermo Fisher Helios) by creating shorts between inner and outer lines, and removing the free-standing SiN membrane, to ensure the in situ biasing capabilities. The setup is shown schematically in Figure S1.

From the milled platinum foil, a free-standing ≥10 µm×10 µm platinum flake was selected. This flake has been cut free without direct ion-beam exposure of the polished edge and further protecting the edge from re-deposition through the positioning of the lift-out needle. The region of ion-beam illumination was carefully selected, and no full area snapshots were acquired. The flake has then been transferred to form a micro-capacitor with a 4 µm gap between the specimen edge and the counter-electrode. The capacitor and the edge protection principle are depicted in Figure S2.

4.2 | Transmission Electron Microscopy

The electron microscopy data was acquired on an FEI Titan 80–300 G2 ETEM with a CEOS CETCOR image corrector operated at 300 kV and a Gatan Ultrascan 1000 XP CCD.

The thickness was measured in energy-filtered transmission electron microscopy with a Gatan Quantum GIF using the log-ratio technique for a 500 nm × 500 nm field of view. The calculated mean-free-path for platinum is λ_{Pt} = 67.7 nm for 300 kV and 45 mrad collection angle [52]. From this analysis, the specimen thickness is estimated to be 2.5 nm at the front edge of the sample, where the electron holography data was measured.

Drift corrected phase shifting electron holography was used to reconstruct the projected electric potential at the Pt(111)-water interface with one Angstrom spatial resolution and $2\pi/452$ phase sensitivity (corresponding to 2.13 V projected potential) can be achieved as previously reported [25]. Phase shifting electron

16146840, 0, Downloaded from https://advanced.onlinelibrary.wiley.com/doi/10.1002/aenm.202505756 by KIZ der Universitat Ulm, Wiley Online Library on [21/01/2026]. See the Terms and Conditions (https://onlinelibrary.wiley.com/terms-and-conditions) on Wiley Online Library for rules of use; OA articles are governed by the applicable Creative Commons License

holography circumvents the low-pass filtering aperture in the reconstruction process that limits the spatial resolution in conventional off-axis electron holography. Residual imperfections in the first order aberrations of the aberration-corrected instrument are numerically adjusted by amplitude-contrast minimization to ≤ 1 nm defocus uncertainty [53]. A detailed comparison of simulated and acquired phase images with phase shifting holography was carried out in [25]. The influence of aberrations on the observed electron phase peaks arising from water layers is shown in Figure S3.

The PS-EH data, including the necessary reference series, was recorded with a biprism situated in the selected area aperture port. The biprism was operated at a voltage of 250 V. For platinum in [110] zone axis, this is sufficient to separate the sideband signal from the first order Bragg spots and apply the drift correction. About 60 phase-shifted electron holograms with one second exposure time each were acquired for each series. This is a compromise between drift correction within one frame and the performance capabilities of the CCD camera used. The total field of view was 15 nm × 15 nm recorded on 2048 px × 2048 px. All observations were carried out at a beam current density of 3000 e $\mathbf{Å}^{-2}$ s^{-1} for sufficient fringe contrast at the chosen magnification. Identical imaging conditions were used for the HRTEM time-series.

4.3 | Numerical Aberration Correction

Further principles and details of phase shifting electron holography data collection and high resolution reconstruction have been reported in the method paper [25], which also includes the developed source code. The first-order aberrations found by [53] are given in Table S1.

In Figure S3, the influence of varying the residual defocus Δf on the reconstructed phase signal is demonstrated. The focus was optimized on a 0.5 nm × 0.5 nm image region close to the specimen edge. Due to the local thickness variation demonstrated in the main text, the optimized defocus found by the minimum contrast criterion is also a local property. Hence, greater variations of the phase signal with the focus are expected for planes further away from the specimen edge. The thinnest parts of the surface region, the dynamic platinum layer, and the water film are less affected by the defocus variation.

4.4 | Specimen Thickness Determination via Multislice Simulations

Simulated wave functions for Pt [110] have been calculated by multi-slice technique [34]. These simulations include the performance characteristics of the electron gun, as well as the modulation transfer function the CCD camera. For the temporal coherence envelope, we used d_{info} = 0.1 nm according to the value measured by following [54]. Thermal diffuse scattering has been accounted for by frozen lattice simulations with the room temperature Debye-Waller factor, expressed by the isotropic B-factor $B_{iso,Pt}$ = 0.384 $Å^2$ [55]. The resulting phase signal versus the simulated thickness for three different cell-metrics is shown in Figure S7. The influence of dynamic diffraction modulates the linear trend. This is particularly important for specimen thicknesses between 1.5 and 2.5 nm, where depending on the metric, the phase of the exit-wave strongly deviates from the linear trend. We neglected the asymmetric influence of the MTF in electron holography as discussed in the supplementary materials of [25], since the expected distortion is at the limit of the phase sensitivity of the method.

4.5 | Ab-Initio Molecular Dynamics Simulations

We performed periodic density functional theory (DFT) calculations using the software package VASP [56]. Exchange-correlation energies were evaluated within the generalized gradient approximation as suggested by Hammer and Nørskov, namely a revised version of the Perdew-Burke-Ernzerhof (RPBE) functional [57], and the dispersion effects were included within the semi-empirical D3 correction scheme [58–60]. We only considered the D3 pair interactions between molecules and between the molecules and the first layer of metal substrate. The wave functions were expanded up to a cutoff energy of 400 eV using a plane wave basis set. The electronic cores were described by the projector augmented wave (PAW) method [61]. The energies of each ionic step satisfied the convergence criteria of 10^{-6} eV.

The water/Pt(111) interface was modeled by 144 water molecules within a 6 × 6 unit cell on a five-layer Pt(111) slab. Due to the large supercell, the integration over the first Brillouin zone was replaced by a summation just over the Gamma k-point. By adding or removing H atoms to or from the water film, the electrode potential was controlled [40, 62, 63]. In order to model the Pt surface with ad-atoms, they were placed at fcc lattice sites on the surface.

The thermodynamic properties of liquid water were averaged by integrating the Langevin equation at 298 K with a time step of 1 fs. We selected a Langevin friction coefficient of $\gamma = 5$ ps^{-1}. For the pzc, H_3O^+, OH^- simulations on flat Pt(111), we sampled during 40 ps after 5 ps thermalization. For the Pt ad-atom simulations, we sampled during 10 ps after 5 ps thermalization.

Author Contributions

Jonas Lindner: formal analysis, investigation, methodology, software, visualization, writing – original draft, writing – review and editing. **Ulrich Ross**: formal analysis, investigation, methodology, software, writing – review and editing. **Tobias Meyer**: methodology, resources, writing – review and editing. **Sung Sakong**: writing – review and editing. **Axel Gross**: funding acquisition, writing – review and editing. **Michael Seibt**: conceptualization, funding acquisition, project administration, resources, supervision, writing – review and editing. **Christian Jooss**: conceptualization, funding acquisition, project administration, resources, supervision, writing – review and editing.

Acknowledgements

The authors thank Victor Bureau and Tore Niermann for sharing their valuable expertise about off-axis holography in the early stages of this work. The discussions with Juri Barthel about multi-slice simulations are gratefully acknowledged.

Open access funding enabled and organized by Projekt DEAL.

16146840, 0, Downloaded from https://advanced.onlinelibrary.wiley.com/doi/10.1002/aenm.202505756 by KIZ der Universitat Ulm, Wiley Online Library on [21/01/2026]. See the Terms and Conditions (https://onlinelibrary.wiley.com/terms-and-conditions) on Wiley Online Library for rules of use; OA articles are governed by the applicable Creative Commons License

Funding

This work was financially supported by the Deutsche Forschungsgemeinschaft (DFG, German Research Foundation) 217133147/SFB 1073, projects C02, Z02, and 510228793/SFB 1633, project C04. The necessary equipment was provided by the "Collaborative Laboratory and User Facility for Electron Microscopy" (CLUE) at University of Goettingen. Both types of support are gratefully acknowledged. SS and AG acknowledge the support by the Dr. Barbara Mez-Starck Foundation and the computational resources provided by the federal state of Baden Württemberg through the bwHPC initiative and by the German Science Foundation (DFG) under grant no INST40/575-1 FUGG (JUSTUS 2 cluster).

Conflicts of Interest

The authors declare no conflicts of interest.

Data Availability Statement

All data is available in the main text or the supplementary information. The code for phase shifting holography can be found on Github or Goettingen University [64]. The AIMD trajectories of clean and with ions and H coverage are available in Zenodo at https://doi.org/10.5281/zenodo.14795249. All other data are available from the corresponding author upon reasonable request.

References

1. H. V. Helmholtz, "Studien über Electrische Grenzschichten," *Annalen der Physik* 243, no. 7 (1879): 337–382, https://doi.org/10.1002/andp.18792430702.

2. D. L. Chapman, "LI. A Contribution to the Theory of Electrocapillarity," *The London, Edinburgh, and Dublin Philosophical Magazine and Journal of Science* 25, no. 148 (1913): 475–481, https://doi.org/10.1080/14786440408634187.

3. O. Stern, "Zur Theorie Der Elektrolytischen Doppelschicht," *Zeitschrift für Elektrochemie und Angewandte Physikalische Chemie* 30, no. 21-22 (1924): 508–516, https://doi.org/10.1002/bbpc.192400182.

4. M. D. Fayer and N. E. Levinger, "Analysis of Water in Confined Geometries and at Interfaces," *Annual Review of Analytical Chemistry* 3 (2010): 89–107, https://doi.org/10.1146/annurev-anchem-070109-103410.

5. H. Yang, A. Boucly, J. P. Gabathuler, T. Bartels-Rausch, L. Artiglia, and M. Ammann, "Ordered Hydrogen Bonding Structure of Water Molecules Adsorbed on Silver Iodide Particles Under Subsaturated Conditions," *The Journal of Physical Chemistry C* 125, no. 21 (2021): 11628–11635, https://doi.org/10.1021/acs.jpcc.1c01767.

6. A. Hodgson and S. Haq, "Water Adsorption and the Wetting of Metal Surfaces," *Surface Science Reports* 64, no. 9 (2009): 381–451, https://doi.org/10.1016/j.surfrep.2009.07.001.

7. S. Dewan, V. Carnevale, A. Bankura, et al., "Structure of Water at Charged Interfaces: A Molecular Dynamics Study," *Langmuir* 30, no. 27 (2014): 8056–8065, https://doi.org/10.1021/la5011055.

8. S.-J. Shin, D. H. Kim, G. Bae, et al., "On the Importance of the Electric Double Layer Structure in Aqueous Electrocatalysis," *Nature Communications* 13, no. 1 (2022): 174, https://doi.org/10.1038/s41467-021-27909-x.

9. T. W. Hansen and M. Willinger, "From Atomistic to Collective Dynamics: Bridging Gaps in Gas-Phase Electron Microscopy for Catalysis," *MRS Bulletin* 48, no. 8 (2023): 842–851, https://doi.org/10.1557/s43577-023-00596-3.

10. C. Barroo, Z.-J. Wang, R. Schlĺogl, and M.-G. Willinger, "Imaging the Dynamics of Catalysed Surface Reactions by In Situ Scanning Electron Microscopy," *Nature Catalysis* 3, no. 1 (2020): 30–39, https://doi.org/10.1038/s41929-019-0395-3.

11. X. Huang, T. Jones, A. Fedorov, et al., "Phase Coexistence and Structural Dynamics of Redox Metal Catalysts Revealed by Operando TEM," *Advanced Materials* 33, no. 31 (2021): 2101772, https://doi.org/10.1002/adma.202101772.

12. Z.-P. Wu, H. Zhang, C. Chen, G. Li, and Y. Han, *Microstructures* 2, no. 1 (2022), https://doi.org/10.20517/microstructures.2021.12.

13. W. Yuan, B. Zhu, X.-Y. Li, et al., "Visualizing H_2O Molecules Reacting at TiO_2 Active Sites With Transmission Electron Microscopy," *Science* 367, no. 6476 (2020): 428–430, https://doi.org/10.1126/science.aay2474.

14. G. Lole, V. Roddatis, U. Ross, et al., "Dynamic Observation of Manganese Adatom Mobility at Perovskite Oxide Catalyst Interfaces With Water," *Communications Materials* 1, no. 1 (2020): 68, https://doi.org/10.1038/s43246-020-00070-6.

15. E. Ronge, J. Lindner, U. Ross, et al., "Atom Surface Dynamics of Manganese Oxide Under Oxygen Evolution Reaction-Like Conditions Studied by In Situ Environmental Transmission Electron Microscopy," *The Journal of Physical Chemistry C* 125, no. 9 (2021): 5037–5047, https://doi.org/10.1021/acs.jpcc.0c09806.

16. W. Schmickler, "Double Layer Theory," *Journal of Solid State Electrochemistry* 24 (2020): 2175–2176, https://doi.org/10.1007/s10008-020-04597-z.

17. A. Groß and S. Sakong, "Ab Initio Simulations of Water/Metal Interfaces," *Chemical Reviews* 122, no. 12 (2022): 10746–10776, https://doi.org/10.1021/acs.chemrev.1c00679.

18. M. Becker, P. Loche, M. Rezaei, et al., "Multiscale Modeling of Aqueous Electric Double Layers," *Chemical Reviews* 124, no. 1 (2023): 1–26, https://doi.org/10.1021/acs.chemrev.3c00307.

19. M. H. Hansen and J. Rossmeisl, "pH in Grand Canonical Statistics of an Electrochemical Interface," *The Journal of Physical Chemistry C* 120, no. 51 (2016): 29135–29143, https://doi.org/10.1021/acs.jpcc.6b09019.

20. J. Le, M. Iannuzzi, A. Cuesta, and J. Cheng, "Determining Potentials of Zero Charge of Metal Electrodes versus the Standard Hydrogen Electrode From Density-Functional-Theory-Based Molecular Dynamics," *Physical Review Letters* 119, no. 1 (2017): 016801, https://doi.org/10.1103/PhysRevLett.119.016801.

21. S. Nie, P. J. Feibelman, N. Bartelt, and K. Thurmer, "Pentagons and Heptagons in the First Water Layer on Pt(111)," *Physical Review Letters* 105, no. 2 (2010): 026102, https://doi.org/10.1103/PhysRevLett.105.026102.

22. J. Peng, J. Guo, R. Ma, and Y. Jiang, "Water-Solid Interfaces Probed by High-Resolution Atomic Force Microscopy," *Surface Science Reports* 77, no. 1 (2022): 100549, https://doi.org/10.1016/j.surfrep.2021.100549.

23. M. R. Uhlig, D. Martin-Jimenez, and R. Garcia, "Atomic-Scale Mapping of Hydrophobic Layers on Graphene and Few-Layer MoS_2 and WSe_2 in Water," *Nature Communications* 10, no. 1 (2019): 2606, https://doi.org/10.1038/s41467-019-10740-w.

24. K.-I. Amano, K. Suzuki, T. Fukuma, O. Takahashi, and H. Onishi, "The Relationship Between Local Liquid Density and Force Applied on a Tip of Atomic Force Microscope: A Theoretical Analysis for Simple Liquids," *The Journal of Chemical Physics* 139 (2013): 22, https://doi.org/10.1063/1.4839775.

25. J. Lindner, U. Ross, T. Meyer, V. Boureau, M. Seibt, and C. Jooss, "Reconstruction of Angstrom Resolution Exit-Waves by the Application of Drift-Corrected Phase-Shifting Off-Axis Electron Holography," *Ultramicroscopy* 256 (2024): 113880, https://doi.org/10.1016/j.ultramic.2023.113880.

26. J. Lindner, U. Ross, V. Roddatis, and C. Jooss, "Langmuir Analysis of Electron Beam Induced Plasma in Environmental TEM," *Ultramicroscopy* 243 (2023): 113629, https://doi.org/10.1016/j.ultramic.2022.113629.

27. A. Opitz, M. Scherge, S.-U. Ahmed, and J. Schaefer, "A Comparative Investigation of Thickness Measurements of Ultra-Thin Water Films by Scanning Probe Techniques," *Journal of Applied Physics* 101, no. 6 (2007): 064310, https://doi.org/10.1063/1.2712155.

28. M. Lehmann, "Determination and Correction of the Coherent Wave Aberration From a Single Off-Axis Electron Hologram by Means of a Genetic Algorithm," *Ultramicroscopy* 85, no. 3 (2000): 165–182, https://doi.org/10.1016/S0304-3991(00)00054-1.

16146840, 0, Downloaded from https://advanced.onlinelibrary.wiley.com/doi/10.1002/aenm.202505756 by KIZ der Universitat Ulm, Wiley Online Library on [21/01/2026]. See the Terms and Conditions (https://onlinelibrary.wiley.com/terms-and-conditions) on Wiley Online Library for rules of use; OA articles are governed by the applicable Creative Commons License

29. J. T. Cowley and S. Iijima, "Electron Microscope Image Contrast for Thin Crystal," *Zeitschrift für Naturforschung A* 27, no. 3 (1972): 445–451, https://doi.org/10.1515/zna-1972-0312.

30. S. Liu, Z. Zhang, J. Nørskov, and H. Metiu, "The Mobility of Pt Atoms and Small Pt Clusters on Pt(111) and Its Implications for the Early Stages of Epitaxial Growth," *Surface Science* 321, no. 1-2 (1994): 161–171, https://doi.org/10.1016/0039-6028(94)90037-X.

31. E. Ronge, J. Lindner, U. Ross, et al., "Atom Surface Dynamics of Manganese Oxide Under Oxygen Evolution Reaction-Like Conditions Studied by In Situ Environmental Transmission Electron Microscopy," *The Journal of Physical Chemistry C* 125, no. 9 (2021): 5037–5047, https://doi.org/10.1021/acs.jpcc.0c09806.

32. D. Miller, H. Oberg, S. Kaya, et al., "Oxidation of Pt(111) Under Near-Ambient Conditions," *Physical Review Letters* 107, no. 19 (2011): 195502, https://doi.org/10.1103/PhysRevLett.107.195502.

33. M. J. Rost, L. Jacobse, and M. T. Koper, "Non-Random Island Nucleation in the Electrochemical Roughening on Pt(111)," *Angewandte Chemie International Edition* 62, no. 27 (2023): 202216376, https://doi.org/10.1002/anie.202216376.

34. J. Barthel, "Dr. Probe: A Software for High-Resolution STEM Image Simulation," *Ultramicroscopy* 193 (2018): 1–11, https://doi.org/10.1016/j.ultramic.2018.06.003.

35. N. Panagiotides and N. I. Papanicolaou, "Diffusion of Platinum Adatoms and Dimers on Pt(111) Surface by Molecular-Dynamics Simulation," *International Journal of Quantum Chemistry* 110, no. 1 (2010): 202–209, https://doi.org/10.1002/qua.22045.

36. J. Huang, Y. Zhang, M. Li, A. Groß, and S. Sakong, "Comparing Ab Initio Molecular Dynamics and a Semiclassical Grand Canonical Scheme for the Electric Double Layer of the Pt(111)/Water Interface," *The Journal of Physical Chemistry Letters* 14, no. 9 (2023): 2354–2363, https://doi.org/10.1021/acs.jpclett.2c03892.

37. A. E. Mikkelsen, J. Schiøtz, T. Vegge, and K. W. Jacobsen, "Is the Water/Pt(111) Interface Ordered at Room Temperature?," *The Journal of Chemical Physics* 155 (2021): 22, https://doi.org/10.1063/5.0077580.

38. J.-B. Le and J. Cheng, "Modeling Electrified Metal/Water Interfaces From Ab Initio Molecular Dynamics: Structure and Helmholtz Capacitance," *Current Opinion in Electrochemistry* 27 (2021): 100693, https://doi.org/10.1016/j.coelec.2021.100693.

39. D. Liu and C. He, "Peak-Aware Guided Filtering for Spectrum Signal Denoising," *Chemometrics and Intelligent Laboratory Systems* 222 (2022): 104508, https://doi.org/10.1016/j.chemolab.2022.104508.

40. J. Huang, Y. Zhang, M. Li, A. Groß, and S. Sakong, "Comparing Ab Initio Molecular Dynamics and a Semiclassical Grand Canonical Scheme for the Electric Double Layer of the Pt(111)/Water Interface," *The Journal of Physical Chemistry Letters* 14 (2023): 2354–2363, https://doi.org/10.1021/acs.jpclett.2c03892.

41. A. Michaelides, "Density Functional Theory Simulations of Water–Metal Interfaces: Waltzing Waters, a Novel 2D Ice Phase, and More," *Applied Physics A* 85, no. 4 (2006): 415–425, https://doi.org/10.1007/s00339-006-3695-9.

42. R. F. Egerton, P. Li, and M. Malac, "Radiation Damage in the TEM and SEM," *Micron* 35, no. 6 (2004): 399–409, https://doi.org/10.1016/j.micron.2004.02.003.

43. S. Mildner, M. Beleggia, D. Mierwaldt, et al., "Environmental TEM Study of Electron Beam Induced Electrochemistry of Pr 0.64 Ca 0.36 MnO 3 Catalysts for Oxygen Evolution," *The Journal of Physical Chemistry C* 119, no. 10 (2015): 5301–5310, https://doi.org/10.1021/jp511628c.

44. N. Nagatsuka, T. Otsuki, S. Kamibashira, T. Koitaya, and K. Watanabe, "Water Orientation on Platinum Surfaces Controlled by Step Sites," *The Journal of Chemical Physics* 161 (2024): 9, https://doi.org/10.1063/5.0221288.

45. P. Li, Y. Liu, and S. Chen, "Microscopic EDL Structures and Charge–Potential Relation on Stepped Platinum Surface: Insights From the Ab Initio Molecular Dynamics Simulations," *The Journal of Chemical Physics* 156 (2022): 10, https://doi.org/10.1063/5.0080104.

46. X. Lin and A. Groß, "First-Principles Study of the Water Structure on Flat and Stepped Gold Surfaces," *Surface Science* 606, no. 11-12 (2012): 886–891, https://doi.org/10.1016/j.susc.2011.12.015.

47. E. Gongadze and A. Igli˘c, "Decrease of Permittivity of an Electrolyte Solution Near a Charged Surface Due to Saturation and Excluded Volume Effects," *Bioelectrochemistry* 87 (2012): 199–203, https://doi.org/10.1016/j.bioelechem.2011.12.001.

48. E. Gongadze and A. Iglič, "Relative Permittivity in Stern and Diffuse Layers," *Acta Chimica Slovenica* 61, no. 2 (2014): 241–245.

49. R. E. Warburton, A. V. Soudackov, and S. Hammes-Schiffer, "Theoretical Modeling of Electrochemical Proton-Coupled Electron Transfer," *Chemical Reviews* 122, no. 12 (2022): 10599–10650, https://doi.org/10.1021/acs.chemrev.1c00929.

50. Y.-B. Zhuang and A. Pasquarello, "Mechanism of First Proton-Coupled Electron Transfer of Water Oxidation at the BiVO4${\rm BiVO}_4$–Water Interface," *Angewandte Chemie International Edition* 64, no. 32 (2025): 202507071, https://doi.org/10.1002/anie.202507071.

51. H. Wang, Y. Qiao, L. Tang, et al., *Science Bulletin* 70, no. 19 (2025), https://doi.org/10.1016/j.scib.2025.08.036.

52. K. Iakoubovskii, K. Mitsuishi, Y. Nakayama, and K. Furuya, "Thickness Measurements With Electron Energy Loss Spectroscopy," *Microscopy Research and Technique* 71, no. 8 (2008): 626–631, https://doi.org/10.1002/jemt.20597.

53. Z. K. Chen, W. Q. Ming, Y. T. He, et al., "Direct Estimation and Correction of Residual Aberrations in the Reconstructed Exit-Wavefunction of a Crystalline Specimen," *Micron* 157 (2022): 103247, https://doi.org/10.1016/j.micron.2022.103247.

54. J. Barthel and A. Thust, "Quantification of the Information Limit of Transmission Electron Microscopes," *Physical Review Letters* 101 (2008): 200801, https://doi.org/10.1103/PhysRevLett.101.200801.

55. H. X. Gao and L.-M. Peng, "Parameterization of the temperature dependence of the Debye–Waller factors," *Acta Crystallographica Section A Foundations of Crystallography* 55 (1999): 926–932, https://doi.org/10.1107/S0108767399005176.

56. G. Kresse and J. Furthmüller, "Efficient Iterative Schemes for Ab Initio Total-Energy Calculations Using a Plane-Wave Basis Set," *Physical Review B* 54 (1996): 11169–11186, https://doi.org/10.1103/PhysRevB.54.11169.

57. B. Hammer, L. B. Hansen, and J. K. Nørskov, "Improved Adsorption Energetics Within Density-Functional Theory Using Revised Perdew-Burke-Ernzerhof Functionals," *Physical Review B* 59 (1999): 7413–7421, https://doi.org/10.1103/PhysRevB.59.7413.

58. S. Grimme, J. Antony, S. Ehrlich, and H. Krieg, "A Consistent and Accurate Ab Initio Parametrization of Density Functional Dispersion Correction (DFT-D) for the 94 Elements H-Pu," *The Journal of Chemical Physics* 132, no. 15 (2010): 154104, https://doi.org/10.1063/1.3382344.

59. S. Grimme, "Density Functional Theory With London Dispersion Corrections," *Wiley Interdiscip Reviews Computational Molecular Science* 1, no. 2 (2011): 211–228, https://doi.org/10.1002/wcms.30.

60. S. Grimme, A. Hansen, J. G. Brandenburg, and C. Bannwarth, "Dispersion-Corrected Mean-Field Electronic Structure Methods," *Chemical Reviews* 116, no. 9 (2016): 5105–5154, https://doi.org/10.1021/acs.chemrev.5b00533.

61. P. E. Blöchl, "Projector Augmented-Wave Method," *Physical Review B* 50 (1994): 17953, https://doi.org/10.1103/PhysRevB.50.17953.

62. S. Sakong and A. Groß, "The Electric Double Layer at Metal-Water Interfaces Revisited Based on a Charge Polarization Scheme," *The Journal of Chemical Physics* 149, no. 8 (2018): 084705, https://doi.org/10.1063/1.5040056.

63. S. Sakong and A. Groß, "Water Structures on a Pt(111) Electrode From ab Initio Molecular Dynamic Simulations for a Variety of Electrochemical

16146840, 0, Downloaded from https://advanced.onlinelibrary.wiley.com/doi/10.1002/aenm.202505756 by KIZ der Universitat Ulm, Wiley Online Library on [21/01/2026]. See the Terms and Conditions (https://onlinelibrary.wiley.com/terms-and-conditions) on Wiley Online Library for rules of use; OA articles are governed by the applicable Creative Commons License

Conditions," *Physical Chemistry Chemical Physics* 22, no. 19 (2020): 10431–10437, https://doi.org/10.1039/C9CP06584A.

64. J. Lindner and U. Ross, Developed Software @github https://github.com/SrcJonasLindner/phase-shifting-holography or via gro data, accessed November 15, 2023, https://data.goettingen-research-online.de/dataverse/phase-shifting-holography.

Supporting Information

Additional supporting information can be found online in the Supporting Information section.

Supporting File: aenm70649-sup-0001-SuppMat.pdf.

16146840, 0, Downloaded from https://advanced.onlinelibrary.wiley.com/doi/10.1002/aenm.202505756 by KIZ der Universitat Ulm, Wiley Online Library on [21/01/2026]. See the Terms and Conditions (https://onlinelibrary.wiley.com/terms-and-conditions) on Wiley Online Library for rules of use; OA articles are governed by the applicable Creative Commons License